



Metal-organic framework derived dual-metal sites for electroreduction of carbon dioxide to HCOOH

Kaili Yao^{a,b}, Haibin Wang^a, Xiaotao Yang^c, Yan Huang^a, Chendong Kou^a, Tan Jing^d, Songhua Chen^d, Ziyun Wang^e, Yongchang Liu^{a,f}, Hongyan Liang^{a,b,*}

^a School of Materials Science and Engineering, Tianjin University, Tianjin 300350, PR China

^b Key Laboratory of Efficient Utilization of Low and Medium Grade Energy, Ministry of Education, Tianjin University, Tianjin 300350, PR China

^c School of Mechanical Engineering, Tianjin University, Tianjin 300350, PR China

^d College of Chemistry and Material Science, Longyan University, Longyan 364012, PR China

^e School of Chemical Sciences, The University of Auckland, Auckland 1010, New Zealand

^f State Key Lab of Hydraulic Engineering Simulation and Safety, Tianjin University, Tianjin 300354, PR China

ARTICLE INFO

Keywords:

Electrocatalytic CO₂ reduction
Metal-organic framework
Dual-metal sites
HCOOH

ABSTRACT

The electrochemical CO₂ reduction to formic acid (HCOOH) by Bi-based catalysts has been considered an effective way to solve the energy and environmental crisis. However, achieving high selectivity, high current density, and long-term stability for HCOOH production, remains a substantial challenge. Herein, BiIn alloy nanoparticles (NPs), deriving from the bimetallic metal-organic frameworks, exhibit an excellent HCOOH Faradaic efficiency (FE_{HCOOH}) of 92.5% at the current density of 300 mA cm⁻², as well as a production rate of 5170 μmol h⁻¹ cm⁻². Moreover, the BiIn alloy NPs also achieve superior stability that over 25 h with less than 10% FE drop at the current density of 120 mA cm⁻² in a membrane electrode assembly system. *In-situ* spectra and theoretical calculations suggest that the Bi-In dual-metal sites can provide the optimal binding energy to *OCHO intermediate, thus accelerating the CO₂ to HCOOH conversion.

1. Introduction

The electrochemical CO₂ reduction (CO₂R) has the potential for converting CO₂ into value-added fuels and feedstocks [1,2]. Among various CO₂R products, formic acid (HCOOH) has shown more economically viable and great prospect of industrialization due to its high market value per energy (cents/kWh) and stability [3,4]. Meanwhile, HCOOH is used in the fuel cell and hydrogen carrier application, making it more attractive [5]. The catalyst's design for achieving high selectivity and activity as well as stability of HCOOH production is of crucial importance [6]. Up to now, the p-block transition metals (e.g., Bi [7,8], Sn [9,10], In [11,12], and Pb [13]) have been reported to be efficient catalysts for electrochemical convert CO₂ into HCOOH [14]. Bi-based catalysts (Bi₂O₃, Bi, etc.) are attractive candidates due to their low cost, non-toxic, and appropriate electronic configuration [15,16]. Recently, MOFs-derived catalysts have attracted much attention in the CO₂R field due to the high surface area, porous structure, and abundant unsaturated metal sites [17]. For example, MOFs derived Bi₂O₃@C catalyst exhibits a Faradaic efficiency for HCOOH (FE_{HCOOH}) of 93%

[18] and MOFs derived Bi₂O₃CO₃ catalyst also shows a FE_{HCOOH} of 96.1% [19]. Even though a range of FE_{HCOOH} production from 80% to 95% has been reported on various Bi-based catalysts [20–22], the low current density (< 200 mA cm⁻²) or stability (< 20 h) remains a challenge [23,24].

Bi has weak binding energy for *OCHO, which makes it difficult to promote HCOOH generation. Combining more than one element in the form of binary or multi-component catalysts is an effective approach to possess suitable binding energy to O, thus enhancing the adsorption of *OCHO intermediate through the interface effect [25], compressive strain [26], and orbital interaction effects [27]. Recent studies reported that improved selectivity for HCOOH has been observed with binary Bi-based catalysts containing Sn [28] and Ce [29] as the second metal, while a decrease in FE_{HCOOH} has been observed with Cu-containing catalyst [30], indicating that the FE_{HCOOH} is sensitive to the elemental composition of Bi-based bimetallic catalysts. In has stronger binding energy for *OCHO, which favors the CO₂-to-HCOOH conversion [31]. For example, the atomic dispersion indium sites reach a turnover frequency of HCOOH as high as 26,771 h⁻¹ [32], the single-atom In-N₄

* Corresponding author at: School of Materials Science and Engineering, Tianjin University, Tianjin 300350, PR China.

E-mail address: hongyan.liang@tju.edu.cn (H. Liang).

<https://doi.org/10.1016/j.apcatb.2022.121377>

Received 10 February 2022; Received in revised form 1 April 2022; Accepted 3 April 2022

Available online 7 April 2022

0926-3373/© 2022 Elsevier B.V. All rights reserved.

sites on metal-organic frameworks (MOFs) derived N-doped carbon matrix display a FE_{HCOOH} of 96% [33] and bimetallic In_xCu_y nanoparticle (NP) catalysts obtain a FE_{HCOOH} of 90% [31], indicating In is also a promising candidate in HCOOH production. However, studies on Bi and In two-component as the HCOOH produce catalyst has never been studied.

An ideal CO_2 to HCOOH catalyst should comprise favorable reactive sites for CO_2 activation and *OCHO intermediates adsorption. It was reported that, with conventional metal or metal oxide electrocatalysts, the surface single metal sites tend to bond weakly with the C or O atom of adsorbed CO_2 and intermediates [34]. Compared with single metal sites, the design of bimetallic sites may not only regulate the electronic structure by the interaction of adjacent metal atoms [35] but also give a more stable intermediate along reaction pathway and less energy to activate the CO_2 molecular [36,37]. In this case, constructing dual-metal sites could provide a new strategy to develop highly efficient catalysts for HCOOH production.

Herein, we report the synthesis of BiIn alloy NPs derived from the bimetallic MOFs. The BiIn alloy NPs obtain the maximum FE_{HCOOH} of 97.8% at -0.92 V vs RHE (reversible hydrogen electrode), and a FE_{HCOOH} of 92.5% at the current density of 300 mA cm^{-2} with a production rate of $5170\text{ }\mu\text{mol h}^{-1}\text{ cm}^{-2}$. Moreover, BiIn alloy NPs achieve a long-term operation for over 25 h in a membrane electrode assembly (MEA) at the current density of 120 mA cm^{-2} that maintains the selectivity exceeding 80%, outperforming most catalysts. Density functional theory (DFT) calculations and *in-situ* spectra reveal that the Bi-In dual-metal sites promote the activation of CO_2 and provide near-optimal binding energy to *OCHO . The newly formed density states strengthen the orbital interaction between the dual-metal sites with the *OCHO intermediate, thus boosting the selectivity and activity as well as the stability for HCOOH production.

2. Experiment section

2.1. Materials and reagents

Bismuth (III) nitrate pentahydrate ($Bi(NO_3)_3 \cdot 5H_2O$), indium(III) chloride ($InCl_3$) were purchased from Aladdin. Nafion solution (5.0 wt %), 1,3,5-benzenetricarboxylic acid (H_3BTC), dimethyl sulfoxide (DMSO), and deuterium oxide (D_2O) were purchased from Sigma-Aldrich. N, N-dimethylformamide (DMF), potassium hydroxide (KOH), methanol (MeOH), and isopropanol (IPA) were purchased from Macklin. All chemicals were used directly without further treatment.

2.2. The preparation of catalysts

2.2.1. Synthesis of MOFs

We first synthesized Bi-MOF by a solvothermal method refer to previous work [6], and then followed by ion exchange to obtain the bimetallic MOFs. Typically, for In-Bi-MOF, 121 mg Bi-MOF, 66 mg $InCl_3$, and 750 mg H_3BTC were added into a 60 mL mixed solution (DMF: MeOH = 4: 1). This mixed solution was sonicated for 20 min until all reactants were dissolved. Then the solution was transferred into a 100 mL Teflon-lined stainless-steel autoclave and heated to $120\text{ }^\circ\text{C}$ for 24 h. The white products were collected by centrifugation and washed with methanol three times, and then dried at $60\text{ }^\circ\text{C}$ overnight under vacuum. The In2-Bi-MOF was obtained by adding 121 mg Bi-MOF, 132 mg $InCl_3$, and 750 mg H_3BTC into the DMF-MeOH mixture, the In-Bi2-MOF was obtained by adding 121 mg Bi-MOF, 33 mg $InCl_3$, and 750 mg H_3BTC into the DMF-MeOH mixture, the following steps were consistent with the synthesis of In-Bi-MOF. The In-MOF was obtained by adding 66 mg $InCl_3$ and 750 mg H_3BTC into the DMF-MeOH mixture, the following steps were also consistent with the synthesis of In-Bi-MOF.

2.2.2. Synthesis of BiIn NPs

The synthesis of BiIn alloy NPs involved an electrochemical

reduction process using In-Bi-MOF as the precursor. 5 mg (or 10 mg) of the In-Bi-MOF was dispersed in a mixture of 950 μL 2-propanol and 50 μL 5 wt% Nafion solution, then sonicated for at least 1 h. The ink was dropped onto a glassy carbon electrode (or spray onto $2 \times 4\text{ cm}$ carbon paper) with a loading of $\sim 0.5\text{ mg cm}^{-2}$ (or $\sim 0.6\text{ mg cm}^{-2}$). The loading was determined by measuring the weight of the glassy carbon (or carbon paper) before and after deposition. The BiIn alloy NPs are obtained by electrochemical reduction of the In-Bi-MOF, which are electro-reduced by consecutive cyclic voltammetry (CV) scans at 50 mV s^{-1} for 20 cycles from -0.3 V to -1.4 V vs RHE in CO_2 -saturated 0.1 M KHCO_3 , until the CV curves became stable and the obtained catalysts exhibited the metallic phase and black color. The $BiIn_2$ alloy NPs and Bi_3In_5 alloy NPs are obtained by the same electrochemical reduction of the In2-Bi-MOF and In-Bi2-MOF, respectively.

2.3. Characterization

The phase of catalysts powder was verified by X-ray diffraction (XRD) with a Bruker D8 Advanced diffractometer using $Cu\text{ K}\alpha$ radiation ($\lambda = 1.5406\text{ \AA}$). The surface morphology of the catalysts was characterized by scanning electron microscopy (SEM, Hitachi S-4800). Transmission electron microscope (TEM) and high-resolution TEM (HRTEM) measurements were performed on a JEOL JEM-2100F instrument operated at 200 kV with an energy-dispersive X-ray system (EDS). X-ray photoelectron spectroscopy (XPS) for surface element investigation was carried out on a Kratos Axis Supra XPS system.

In-situ attenuated total reflection-Fourier-transform infrared (ATR-FTIR) spectra were measured using a Thermo Scientific Nicolet iS50 FTIR spectrometer with a liquid N_2 cooled Mercury Cadmium Telluride (MCT) detector, coupled to a Pike VeeMAX III attachment. 5 mg of the catalyst was dispersed in a 950 μL 2-propanol with 50 μL Nafion solution. After sonicating the dispersion for 1 h, it was drop coated on Au film with a catalyst loading of $\sim 0.5\text{ mg cm}^{-2}$. Spectra were recorded with a resolution of 4 cm^{-1} in a CO_2 -saturated $0.1\text{ M KHCO}_3\text{-D}_2\text{O}$ electrolyte at applied potentials from OCP to -0.9 V vs RHE, with the spectrum collected at OCP serving as the baseline.

2.4. Catalytic activity evaluation

The CO_2 R catalytic performance of the prepared BiIn alloy NPs, Bi NPs, and In NPs were firstly conducted in a CO_2 -saturated 0.1 M KHCO_3 electrolyte using a gas-tight two-compartment H-cell. The glassy carbon electrode was used as the working electrode, a platinum mesh and an Ag/AgCl electrode were used as the counter electrode and reference electrode, respectively. A proton exchange membrane (Nafion 117) was used to separate the cathode and anode compartments. A gas chromatograph (GC-2060A) equipped with a thermal conductivity detector (TCD) and a flame ionization detector (FID) was used to analyze the gas products of CO_2 reduction (H_2 , CO). Nitrogen (99.999%) was used as the carrier gas. ^1H NMR spectrum (Bruker, AVANCE IIIITM HD 400 MHz) was used to determine the liquid products (HCOOH) in 10% D_2O using water suppression mode, with dimethyl sulfoxide as an internal standard.

The CO_2 R performance of the catalysts was also investigated in 1.0 M KOH electrolyte by using a flow-cell configuration, which comprised of spray-coated gas diffusion layer as the cathode, an anion exchanged membrane (AEM, Fumasep FAA-3-PK-130) as the membrane, Ni foam as the anode, and Ag/AgCl was used as the reference electrode. CO_2 gas flowed behind the gas diffusion layer at a rate of 50 standard cubic centimeters per minute (sccm). The performance of the cathodes was evaluated by performing constant-current electrolysis from 50 mA cm^{-2} to 300 mA cm^{-2} in an electrochemical workstation (CHI 660E). The electrode potentials were converted to values regarding the RHE using the following equation:

$$E_{RHE} = E_{Ag/AgCl} + 0.197\text{ V} + 0.0591\text{ V} \times \text{pH} + 85\% \times i \times R$$

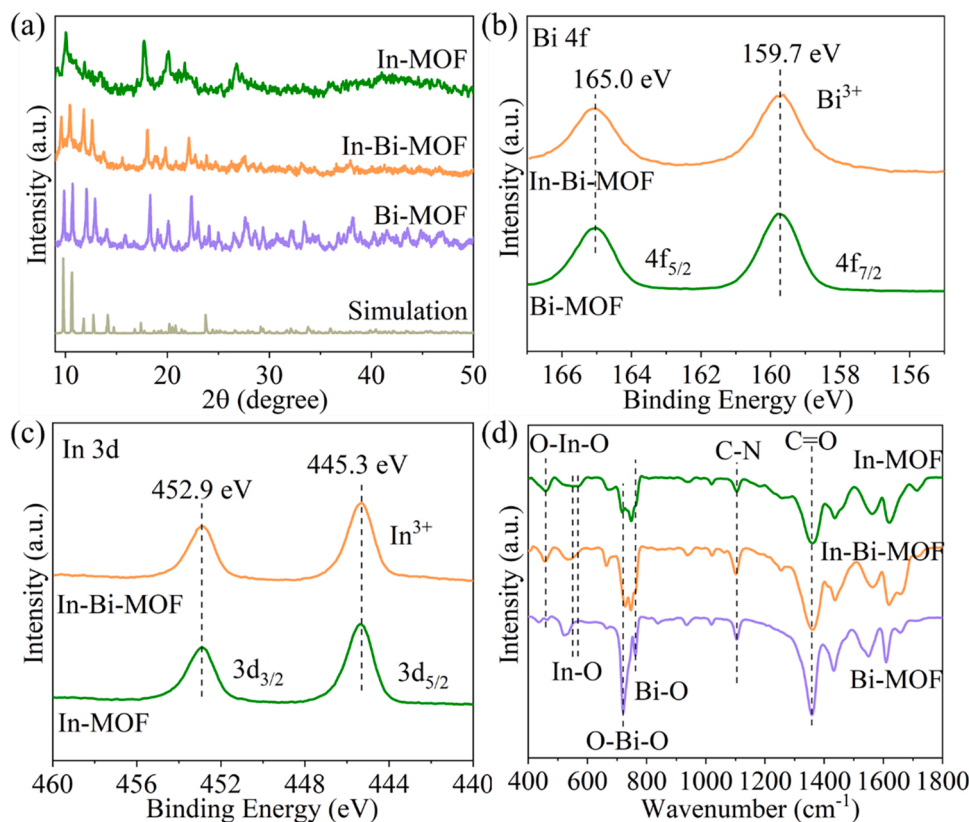


Fig. 1. (a) XRD patterns for Bi-MOF, In-Bi-MOF, In-MOF, and simulated Bi-MOF data from crystals, (b) Bi 4f XPS spectra of Bi-MOF and In-Bi-MOF, (c) In 3d XPS spectra of In-MOF and In-Bi-MOF, and (d) FTIR spectra of Bi-MOF, In-Bi-MOF and In-MOF.

where the ohmic loss (R) between the working and reference electrodes was measured using the electrochemical impedance spectroscopy technique (EIS, frequency ranges from 100 kHz to 0.1 Hz and amplitude of 10 mV). To measure the double-layer capacitance (C_{dl}) from CV, we scanned the CV curves at a non-Faradaic region of -0.48 to -0.6 V vs Ag/AgCl with different scan rates.

The stability performance for Bi-In alloy NPs was evaluated in an MEA system, which was comprised of cathode and anode flow field plates with a flow field of 4 cm^2 . An iridium oxide deposited titanium foam as the anode [38], catalysts sprayed onto a carbon paper as the cathode, which was separated by an anion-exchange membrane (AEM, Sustainion X37-50 grade 60 membrane). The continuous supply of anolyte (0.1 M KHCO_3) with a flow rate of 15 mL min^{-1} and the humidified CO_2 was supplied from the gas diffusion electrode back with a constant flow rate of 68 sccm. The catalytic performance was carried out by applying a constant current density of 120 mA cm^{-2} to the cathode. The liquid products are collected every few hours for NMR detection and replaced with fresh CO_2 -saturated KHCO_3 to mitigate the pH effects. It should be noted that the reaction will be restarted at the 27th hour which is limited by the electrochemical station.

2.5. Theoretical calculation details

All the DFT calculations were performed using the Vienna *ab initio* Software (VASP) [39,40]. The generalized gradient approximation (GGA) with Perdew, Burke, and Ernzerhof (PBE) functional is adopted to describe the electron exchange-correlation interaction [41,42]. Electron wave functions are expanded in plane waves with a kinetic energy cutoff of 400 eV. The method of Methfessel-Paxton (MP) with a smearing width of 0.20 eV was employed to transition metal surfaces and interfaces [43]. The convergence criteria for the electronic self-consistent iteration energy and force were set to 10^{-5} eV and 0.05 eV \AA^{-1} ,

respectively. A vacuum layer of 15 \AA was introduced to avoid the interactions between periodic images. All the slabs are four layers, the bottom two layers are fixed while the upper two layers were relaxed during optimization. $(3 \times 3 \times 1)$ k-point grid was used as three models for DFT calculations. For Gibbs free energy, the following equation was used:

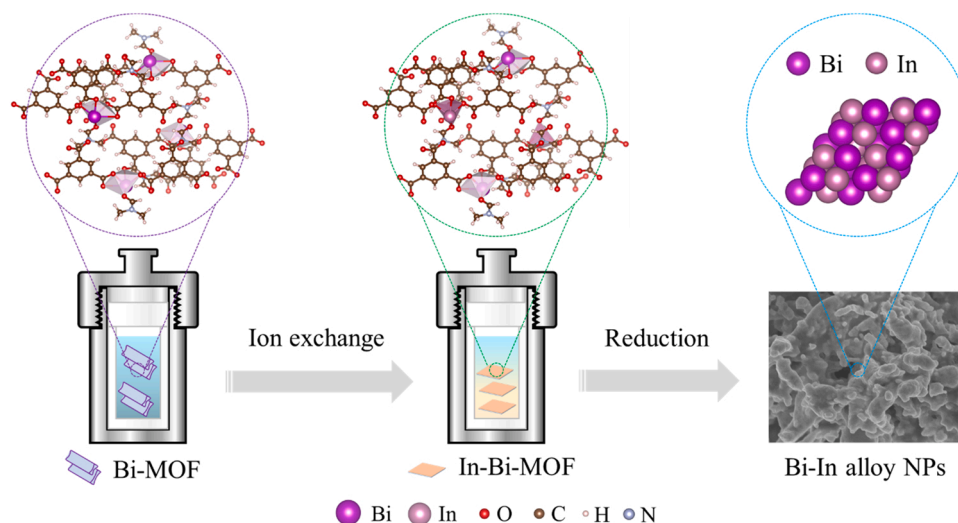
$$G = H - TS = E_{\text{DFT}} + E_{\text{ZPE}} + \int_0^{298} C_p dT - TS$$

where E_{DFT} is the electronic energy and E_{ZPE} is the zero-point vibrational energy. The third and the fourth terms are heat capacity and correction to entropy, respectively, obtained from frequency calculations. The following corrections were applied to partially counterbalance the overestimation from DFT calculations [28]: CO_2 (0.45 eV), H_2 (-0.09 eV), and HCOOH (0.20 eV).

3. Results and discussion

3.1. Characterizations of the In-Bi-MOF

SEM and TEM images in Fig. S1 show that In-Bi-MOF has a nanosheet morphology, and Bi, In, C, and O elements are uniformly distributed over the entire MOF structure. The XRD pattern of In-Bi-MOF matches well with that of Bi-MOF [44], suggesting these mixed-metal MOFs retain the Bi-MOF structure (Fig. 1a). As further investigated by XPS, the oxidized Bi^{3+} at around 165.0/159.7 eV are observed both in Bi-MOF and In-Bi-MOF (Fig. 1b) [4], and the peak profile of In 3d (452.9/445.3 eV) indicates that In^{3+} species is the main component of both In-MOF and In-Bi-MOF (Fig. 1c) [12]. XRD and XPS results imply that the In^{3+} could be incorporated into the framework of Bi-MOF through an ion exchange process by partially replacing Bi^{3+} and binding with BTC^{3-} ligand. The surface functional groups and the formation



Scheme 1. Illustration of the synthetic process for BiIn alloy NPs derived from the In-Bi-MOF.

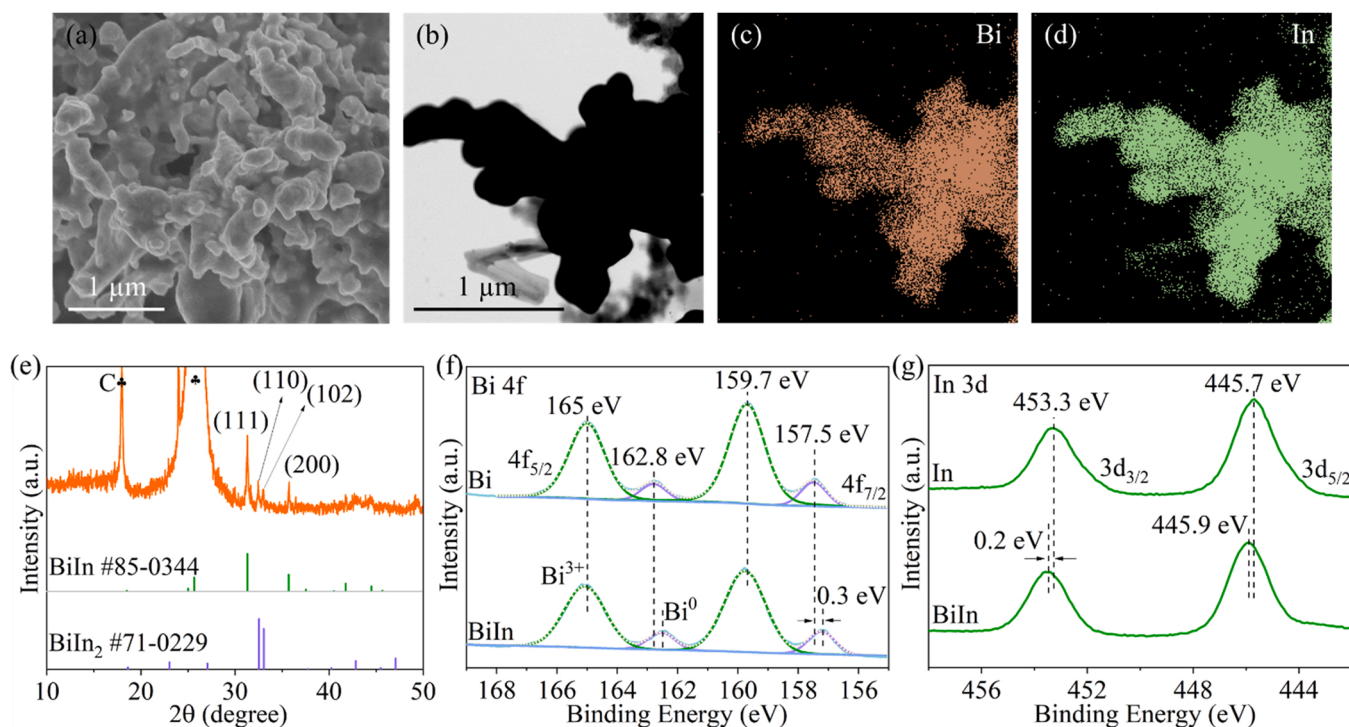


Fig. 2. (a) SEM image, (b) STEM image, EDS elemental mapping images of (c) Bi element and (d) In element, and (e) XRD pattern of BiIn alloy NPs. (f) Bi 4f XPS spectra of BiIn alloy NPs and Bi NPs. (g) In 3d XPS spectra of BiIn alloy NPs, and In NPs.

of coordinated polymers in In-Bi-MOF are further confirmed by FTIR spectra (Fig. 1d). For Bi-MOF, it can be observed that the peaks at $1400\text{--}1614\text{ cm}^{-1}$ are assigned to aromatic carbons, and a small peak of 1103 cm^{-1} is identified as C-N stretching vibration modes that possibly originated from the addition of a small amount of DMF during the preparation process [45]. With the vibrations of O-Bi-O groups at $600\text{--}800\text{ cm}^{-1}$, there is an intense peak at 764 cm^{-1} and can be assigned to Bi-O stretching both in Bi-MOF and In-Bi-MOF. After the addition of In^{3+} , the bonds attributed to In-O ($535/560\text{ cm}^{-1}$) and O-In-O (450 cm^{-1}) are also observed both in In-Bi-MOF and In-MOF [46]. The FTIR results infer the successful preparation of a bimetallic In-Bi-MOF.

3.2. Characterization of the BiIn NPs

The BiIn alloy NPs are obtained by electrochemical reduction of the In-Bi-MOF (Scheme 1). As the controls, Bi NPs (Fig. S2) and In NPs (Fig. S3) are also obtained by electrochemical reduction of the Bi-MOF and In-MOF, respectively. As shown in Fig. 2a, the BiIn alloy NPs display a dendritic-like morphology and the diameter of the branches is about $70\text{--}100\text{ nm}$, consistent with the results of the TEM image (Fig. 2b). HRTEM images reveal that the lattice spacings are 0.285 nm and 0.251 nm , corresponding to the (111) and (200) planes of BiIn, and two sets of diffraction spots can be observed, further demonstrating the phase of BiIn alloy (Fig. S4). The EDS mapping of BiIn alloy NPs confirms that the Bi and In elements are uniformly distributed with the atomic ratio of $1:1.16$ (Fig. 2c-d and Fig. S4). Also, XRD patterns clearly show

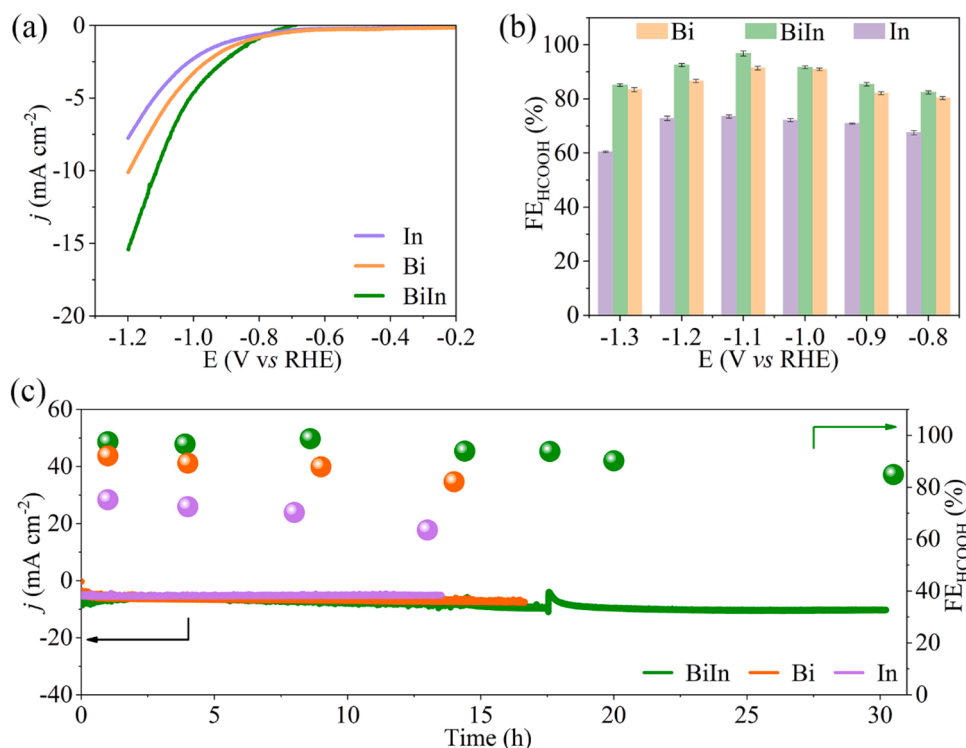


Fig. 3. The catalytic performance of catalysts in H-cell. (a) LSVs of BiIn alloy NPs, Bi NPs, and In NPs in CO₂-saturated 0.1 M KHCO₃. (b) Comparison FEs of HCOOH over the BiIn alloy NPs, Bi NPs, and In NPs at various applied potentials. (c) Durability test of the BiIn alloy NPs, Bi NPs, and In NPs.

that the emergence of BiIn alloy peaks at 31.3° and 35.7°, which are indexed to the (111) and (200) planes of the tetragonal BiIn (JCPDS#85-0344), and two small peaks at 32.5° and 33.1° are attributed to the hexagonal BiIn₂ (JCPDS#71-0229) (Fig. 2e) [47].

XPS is performed to further investigate the composition and valence state of the catalysts. As shown in Fig. 2f and g, in BiIn alloy NPs, the XPS peaks of Bi 4f shift towards lower binding energy direction compared with that of Bi NPs, and the XPS peaks of In 3d shift towards higher binding energy direction compared with that of In NPs, indicating the electron transfer from In to Bi. For the Bi 4f XPS spectra (Fig. 2f), the peaks located at 162.5 eV and 157.2 eV are ascribed to the metallic Bi, and the other two peaks are contributed to Bi³⁺ [48]. The Bi³⁺ peaks are ascribed to the surface oxidation when exposed to air. For the In 3d XPS spectra (Fig. 2g), because the peak location of In³⁺ and In⁰ are very close ($\Delta E = 0.2$ eV), it is difficult to divide these peaks accurately. The XPS spectra prove the electronic interactions between In and Bi in BiIn alloy NPs.

3.3. Catalytic performance of the BiIn NPs

The CO₂R catalytic performance of the prepared BiIn alloy NPs, Bi NPs, and In NPs is conducted in the CO₂-saturated 0.1 M KHCO₃ electrolyte using a gas-tight two-compartment H-cell. We first test the line sweep voltammetry (LSV) curves, the results show that the BiIn alloy NPs has the more positive potential and larger current density for CO₂R (Fig. 3a). To quantify the FE_{HCOOH}, all the catalysts are subsequently evaluated in a chronoamperometry mode. As shown in Fig. 3b, the FEs of HCOOH of BiIn alloy NPs, Bi NPs, and In NPs all increase and then decline when the potential increase. The BiIn alloy NPs reach the maximum value of FE_{HCOOH} for 97.6% at -1.1 V vs RHE, which is higher than the Bi NPs of 92.1% and In NPs of 75.2%. While increasing the potentials, the FE_{HCOOH} decrease, which is probably due to the limited mass transport of reactants. To confirm the HCOOH production comes from the CO₂ rather than the decomposition from the incomplete reduction of MOF structure, we conduct the reduction reaction test in

N₂-saturated 0.1 M KHCO₃. NMR results show that the HCOOH is not detected in the N₂ condition (Fig. S5a), indicating the HCOOH is produced by the electroreduction of CO₂. Besides, we also compared the HCOOH selectivity for the catalysts with different reduction degrees. As shown in Fig. S5b, the pristine In-Bi-MOF without pretreatment (0 cycles of CV) shows a FE_{HCOOH} of 35.2%, the partial reduced In-Bi-MOF (5 cycles of CV) has a FE_{HCOOH} of 90.7%, both of which are lower than that (97.6%) of the completely reduced In-Bi MOF (20 cycles of CV).

Furthermore, a long-term HCOOH production test was performed at -1.1 V vs RHE to assess the durability of the BiIn alloy NPs. During the CO₂R process, the liquid products are collected every few hours for NMR detection and replaced with fresh CO₂-saturated KHCO₃ to mitigate the pH effects. As shown in Fig. 3c, the BiIn alloy NPs show a FE_{HCOOH} exceeding 90% for over 20 h and also keep a FE_{HCOOH} > 85% when extending the time to 30 h. Meanwhile, the current density presents no significant degradation, confirming the stable performance of BiIn alloy NPs. However, the FE_{HCOOH} for Bi NPs and In NPs decline obviously within 15 h, dropping from 92.1% to 82.1% (Bi NPs) and 75.2–63.5% (In NPs), respectively.

The catalytic performance of BiIn alloy NPs, Bi NPs, and In NPs for the CO₂R are also measured in a flow-cell using 1.0 M KOH as the electrolyte, as that flow-cell could increase the mass transfer and the alkaline electrolyte could suppress the hydrogen evolution reaction (HER) [49]. LSV curves demonstrate that much higher current density responses and a more positive potential are observed for BiIn alloy NPs compared to those of the Bi NPs and In NPs, implying the better CO₂R performance for BiIn alloy NPs (Fig. 4a). Furthermore, as shown in Fig. 4b, the BiIn alloy NPs shows over 90% FE_{HCOOH} in a wide range of current densities with an optimum peak of 97.8% at the current density of 250 mA cm⁻², and only a small amount of H₂ and CO was detected (Fig. S6). Moreover, a partial current density of HCOOH up to 278 mA cm⁻² at the potential of -0.95 V can be achieved over BiIn alloy NPs, which is higher than that of Bi NPs (249.6 mA cm⁻², -1.12 V) and In NPs (161.4 mA cm⁻², -1.33 V) (Fig. 4c). Therefore, the production rate of HCOOH over BiIn alloy NPs can reach

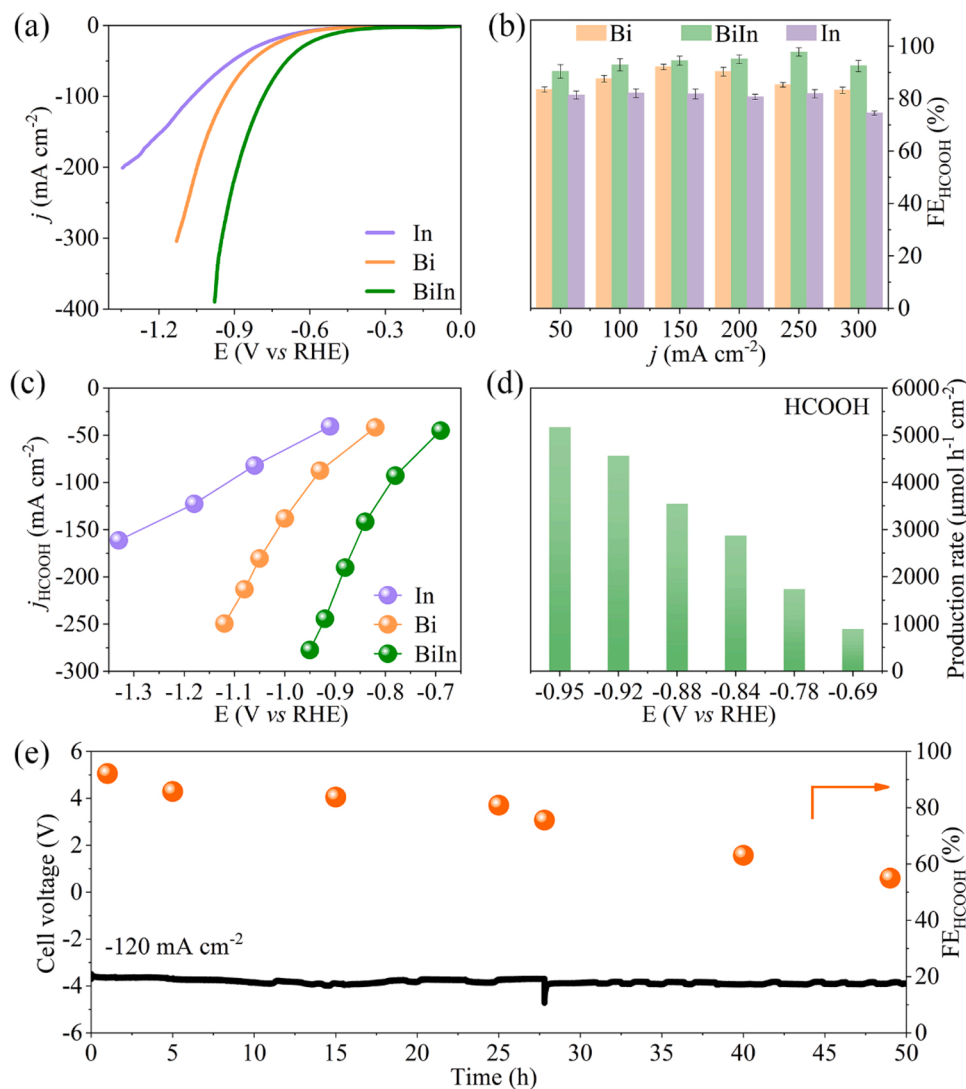


Fig. 4. The catalytic performance of catalysts in flow-cell. (a) LSV results for BiIn alloy NPs, Bi NPs, and In NPs in 1.0 M KOH. (b) Comparison FEs of HCOOH for the BiIn alloy NPs, Bi NPs, and In NPs at various current densities. (c) Partial current densities of HCOOH for BiIn alloy NPs, Bi NPs, and In NPs at different potentials. (d) Production rate of HCOOH over BiIn alloy NPs at various potentials. (e) Long-term chronopotentiometry result and the FEs of HCOOH over BiIn alloy NPs in an MEA (4 cm² electrode).

5170 μmol h⁻¹ cm⁻² at -0.95 V (300 mA cm⁻²) with a FE of 92.5% (Fig. 4d).

Moreover, we also investigated the catalytic performance of different molar ratios between Bi and In under different current densities. It is shown that the BiIn alloy NPs has the highest FE_{HCOOH} of 97.8% relative to the 94.9% of BiIn₂ alloy NPs (Fig. S7) and 86.8% of Bi₃In₅ alloy NPs (Fig. S8) at the current density of 250 mA cm⁻², verifying that the prepared BiIn alloy NPs possesses the better selectivity than the other composites. In addition to electrocatalytic properties, stability at high current density is also an important parameter in the practical application of synthetic electrocatalysts. The BiIn alloy NPs is carried out through a long-term chronopotentiometry at 120 mA cm⁻² in an MEA system using 0.1 M KHCO₃ as the electrolyte. BiIn alloy NPs show an initial FE_{HCOOH} exceeding 92% and the FE_{HCOOH} have no obvious decrease over 25 h (Fig. 4e). After 27 h, the FE_{HCOOH} decreased rapidly, which may be caused by the three factors: (i) the formed carbonate plugged the gas diffusion layer, resulting in the increased HER [50]; (ii) the decreased hydrophobicity of the carbon paper led to the overflow of electrolyte and reduced the diffusion of CO₂, resulting in a decreased mass transfer at high current density [51]; (iii) the produced HCOOH could cross the anion exchange membrane and get re-oxidized by the anode [52]. Besides, the fluctuation of activity stability for BiIn NPs may be attributed to the turbulence of electrolyte circling, the CO₂ flowing, as well as the local pH changing during the long-term testing [28], and

the fluctuation at the 27th hour may be caused by the electrode polarization when restarted of the electrochemical test. However, the morphology change is negligible and the phase of BiIn alloy NPs has not changed after the stability test (Fig. S9). The above catalytic results suggest that the BiIn alloy NPs outperform the recently reported catalysts for HCOOH production (Fig. S10 and Table S1).

To better understand the origin of the enhanced selective and active for BiIn alloy NPs, electrochemical active surface area (ECSA) is evaluated by calculating the C_{dl} . The value of C_{dl} was determined by CV at different rates in a CO₂-flowed 1.0 M KOH electrolyte (Fig. S11a-c). BiIn alloy NPs possess a higher capacitance (1.03 mF cm⁻²) than that of Bi NPs (0.58 mF cm⁻²) and In NPs (0.42 mF cm⁻²) (Fig. S11d), demonstrating that BiIn alloy NPs owns richer active sites. To identify the intrinsic electrocatalytic activity, we normalized the partial current density of HCOOH by the ECSA. BiIn alloy NPs show a higher partial current density (250 mA mF⁻¹) than Bi NPs (150 mA mF⁻¹) and In NPs (100 mA mF⁻¹) (Fig. S12), indicating the enhanced intrinsic activity of BiIn alloy NPs. We also carried out EIS to determine the charge-transfer ability. As shown in Fig. S13, BiIn alloy NPs displayed a smaller diameter of the semicircle concerning the Bi NPs and In NPs, indicating the lower charge-transfer resistance. These results confirm that catalysts with two-component exhibit higher selectivity than the single metal catalysts.

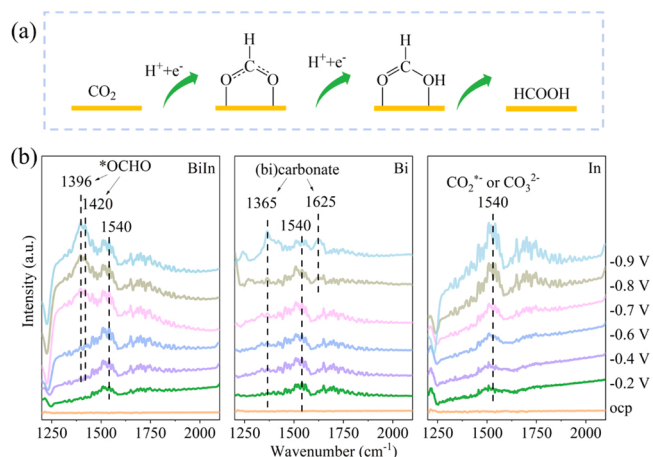


Fig. 5. (a) Illustration of the reaction pathway for the generation of HCOOH. (b) *in-situ* ATR-FTIR spectra of BiIn alloy NPs, Bi NPs, and In NPs at various potentials.

3.4. Catalytic mechanisms of the BiIn NPs

A typical CO_2R process to HCOOH can be described as follows [31]: firstly, the adsorbed CO_2 molecules obtained the electron (e^-) and proton (H^+) to form the $^*\text{OCHO}$ intermediate (where * represents the adsorbed species or surface site); then, $^*\text{OCHO}$ further react with e^- and H^+ to produce $^*\text{HCOOH}$; finally, the $^*\text{HCOOH}$ desorbing from the surface to generate the HCOOH product (Fig. 5a).

To directly link the enhanced selectivity for HCOOH to the BiIn alloy NPs, we carried out *in-situ* ATR-FTIR to monitor the intermediate species adsorbed on the catalysts [53]. As shown in Fig. 5b, we collected the spectra at different applied potential from open circuit potential (OCP) to -0.9 V in a CO_2 -saturated 0.1 M KHCO_3 D_2O electrolyte. At more negative potentials, BiIn alloy NPs show the peaks at 1396 cm^{-1} and 1420 cm^{-1} , which can be assigned to the symmetric stretching mode of

O-C-O in two-oxygen bridged $^*\text{OCHO}$ species [25,54]. Bi NPs display peaks at 1365 cm^{-1} and 1625 cm^{-1} that are ascribed to the surface (bi) carbonate anions [53], but no peaks located at 1360–1430 cm^{-1} are detected for In NPs, indicating $^*\text{OCHO}$ is the key intermediate for HCOOH produce. In addition, peaks at 1540 cm^{-1} can be attributed to asymmetric C-O stretching vibration modes of the CO_2^* intermediate or adsorbed CO_3^{2-} species [55], which may come from the adsorbed CO_2 molecules. It can be seen that the three catalysts all exhibit the peak at 1540 cm^{-1} , indicating the lower potential for CO_2 adsorption. These results suggest that BiIn alloy NPs are beneficial for CO_2 adsorption and have a stronger binding ability with the $^*\text{OCHO}$ than Bi NPs.

To understand the fundamental mechanism for the high HCOOH selectivity on BiIn alloy NPs, we conduct the DFT to calculate the free energies of each reaction step from the CO_2 to HCOOH on Bi (003), BiIn (200) and In (101). The optimized adsorption configurations of reactants, intermediates, and products on catalysts are displayed in Fig. 6a–d and Fig. S14, and the calculated results are summarized in Table S2.

As shown in Fig. 6e, initially, all the three catalysts can spontaneously adsorb CO_2 to form CO_2^* , and the free energy for BiIn (200) (-0.12 eV) is lower than that of Bi (003) (-0.05 eV). Then, the adsorbed CO_2^* reacts with a proton and an electron to produce the $^*\text{OCHO}$ intermediate, and the reaction free energy of $^*\text{OCHO}$ for BiIn (200) and Bi (003) is 0.05 eV and 0.61 eV, respectively, indicating the stronger adsorption with $^*\text{OCHO}$ of BiIn (200). Noted that this step is the potential limiting step for Bi (003) [28]. The next reaction step is the proton-coupled electron transfer step (from $^*\text{OCHO}$ to $^*\text{HCOOH}$), which is the potential-limiting step for In (101) [31] and BiIn (200), and the latter one has a lower reaction energy (0.32 eV) than that of In (101) (0.66 eV). Hence, we can conclude that: (i) when compared with Bi NPs, BiIn alloy NPs can promote CO_2 adsorption for the formation of $^*\text{OCHO}$; (ii) when compared with In NPs, BiIn alloy NPs can reduce the free energy from $^*\text{OCHO}$ to $^*\text{HCOOH}$. Therefore, BiIn alloy NPs can provide the optimal binding energy with $^*\text{OCHO}$, and then promote the HCOOH generation through the synergistic effect of the Bi-In dual-metal sites.

To illustrate the electronic interaction between the adsorbate and

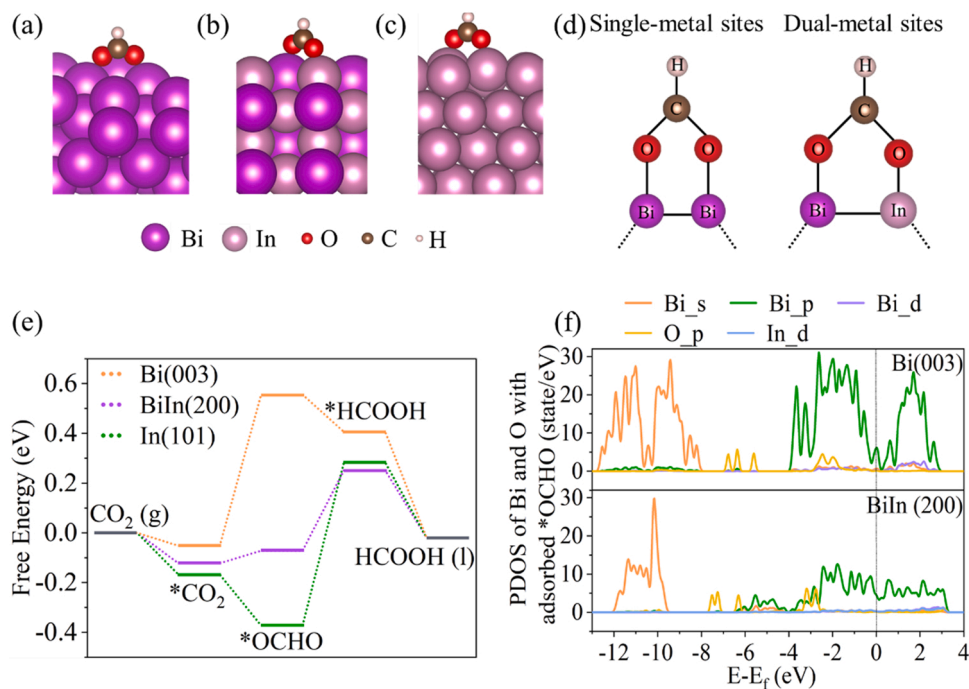


Fig. 6. Optimized adsorption configurations of $^*\text{OCHO}$ intermediates on the surface of the (a) Bi (003), (b) BiIn (200), and (c) In (101). (d) $^*\text{OCHO}$ adsorption in single-metal (left) and dual-metal (right) catalytic systems through side-on configurations. (e) Calculated free energy profiles for CO_2R to HCOOH on Bi (003), BiIn (200), and In (101). (f) PDOS of the s, p, and d orbitals of Bi atoms, p orbitals of O atoms, and d orbitals of In atoms.

catalysts, the projected density of states (PDOS) of BiIn (200) and Bi (003) is calculated (Fig. 6f). Upon the adsorption of *OCHO intermediates, the Bi (003) exhibit the main overlaps between the *p* orbitals of O atoms and *p* orbitals of Bi atoms. For BiIn (200), the new harmonic overlaps between the *p* orbitals of O atoms and *p* orbitals of Bi atoms appeared at energy levels from -4 to -2 eV. The newly formed states in the gap region are expected to facilitate the charge transfer between BiIn and adsorbed *OCHO intermediate, thus promoting the formation of *OCHO on the BiIn (200) surface [27,56]. The theory calculated results indicate that the Bi-In dual-metal sites have stronger binding energy with *OCHO intermediates than the Bi-Bi single-metal sites, thus promoting the formation of *OCHO on the BiIn surfaces.

4. Conclusions

In summary, dual-metal sites on BiIn alloy NPs are explored as an efficient CO₂R catalyst for HCOOH production, and a comprehensive on the electrocatalytic origination are investigated. The BiIn alloy NPs are produced through a solvothermal route using cation exchange and subsequently followed by an electrochemical reduction of MOFs. The BiIn alloy NPs reaches a maximum FE_{HCOOH} of 97.8% at -0.92 V vs RHE, and a FE_{HCOOH} of 92.5% at the current density of 300 mA cm⁻² with a production rate of 5170 $\mu\text{mol h}^{-1} \text{cm}^{-2}$. Moreover, BiIn alloy NPs achieve a long-term operation for over 25 h in an MEA at the current density of 120 mA cm⁻² that maintains the selectivity exceeding 80%. The impressive selectivity, activity, and stability of the BiIn alloy NPs are attributed to the Bi-In dual-metal sites that not only promote the CO₂ adsorption for the formation of *OCHO but also decrease the reaction energy for the formation of *HCOOH, thus improving the CO₂R performance.

CRediT authorship contribution statement

Kaili Yao: Conceptualization, Data curation, Writing – original draft. **Haibin Wang:** Formal analysis, Data curation. **Xiaotao Yang:** Formal analysis, Data curation. **Yan Huang:** Data curation. **Chendong Kou:** Data curation. **Tan Jing:** Funding acquisition. **Songhua Chen:** Funding acquisition. **Ziyun Wang:** Density functional theory advice. **Yongchang Liu:** Formal analysis, Writing – review & editing. **Hongyan Liang:** Supervision, Writing – review & editing, Funding acquisition.

Declaration of Competing Interest

The authors declare that they have no known competing financial interests or personal relationships that could have appeared to influence the work reported in this paper.

Acknowledgments

This work was supported by the National Natural Science Foundation of China (NSFC No. 51771132), an Innovation and Entrepreneurship Training Program for College Students in Fujian Province (S202111312029), and the Open Fund Project of Qinghai Minzu University - Nanomaterials and Nanotechnology Team & Platform (2021GFW-0888).

Declaration of competing interest

The authors reported no declarations of interest.

Appendix A. Supporting information

Supplementary data associated with this article can be found in the online version at doi:10.1016/j.apcatb.2022.121377.

References

- [1] H. Lu, J. Tournet, K. Dastafkan, Y. Liu, Y.H. Ng, S.K. Karuturi, C. Zhao, Z. Yin, Noble-metal-free multicomponent nanointegration for sustainable energy conversion, *Chem. Rev.* 121 (2021) 10271–10366.
- [2] L.M. Wang, W.L. Chen, D.D. Zhang, Y.P. Du, R. Amal, S.Z. Qiao, J.W. Bf, Z.Y. Yin, Surface strategies for catalytic CO₂ reduction: from two-dimensional materials to nanoclusters to single atoms, *Chem. Soc. Rev.* 48 (2019) 5310–5349.
- [3] M.G. Kibria, J.P. Edwards, C.M. Gabardo, C.-T. Dinh, A. Seifitokaldani, D. Sinton, E.H. Sargent, Electrochemical CO₂ reduction into chemical feedstocks: from mechanistic electrocatalysis models to system design, *Adv. Mater.* 31 (2019), 1807166.
- [4] J. Yang, X. Wang, Y. Qu, X. Wang, H. Huo, Q. Fan, J. Wang, L.-M. Yang, Y. Wu, Bi-based metal-organic framework derived leafy bismuth nanosheets for carbon dioxide electroreduction, *Adv. Energy Mater.* 10 (2020), 2001709.
- [5] S. Chatterjee, I. Dutta, Y. Lum, Z.P. Lai, K.W. Huang, Enabling storage and utilization of low-carbon electricity: power to formic acid, *Energy Environ. Sci.* 14 (2021) 1194–1246.
- [6] L. Liu, K. Yao, J. Fu, Y. Huang, N. Li, H. Liang, Bismuth metal-organic framework for electroreduction of carbon dioxide, *Colloid Surf. A* 633 (2022), 127840.
- [7] L. Yi, J. Chen, P. Shao, J. Huang, X. Peng, J. Li, G. Wang, C. Zhang, Z. Wen, Molten-salt-assisted synthesis of bismuth nanosheets for long-term continuous electrocatalytic conversion of CO₂ to formate, *Angew. Chem. Int. Ed.* 59 (2020) 20112–20119.
- [8] F. Li, G.H. Gu, C. Choi, P. Kolla, S. Hong, T.-S. Wu, Y.-L. Soo, J. Masa, S. Mukerjee, Y. Jung, J. Qiu, Z. Sun, Highly stable two-dimensional bismuth metal-organic frameworks for efficient electrochemical reduction of CO₂, *Appl. Catal. B-Environ.* 277 (2020), 119241.
- [9] K. Ye, Z.W. Zhou, J.Q. Shao, L. Lin, D.F. Gao, N. Ta, R. Si, G.X. Wang, X.H. Bao, In situ reconstruction of a hierarchical Sn-Cu/SnO_x core/shell catalyst for high-performance CO₂ electroreduction, *Angew. Chem. Int. Ed.* 59 (2020) 2–10.
- [10] S. Yan, C. Peng, C. Yang, Y. Chen, J. Zhang, A. Guan, X. Lv, H. Wang, Z. Wang, T.-K. Sham, Q. Han, G. Zheng, Electron localization and lattice strain induced by surface lithium doping enable amper-level electrosynthesis of formate from CO₂, *Angew. Chem. Int. Ed.* 60 (2021) 25741–25745.
- [11] X. Kang, B. Wang, K. Hu, K. Lyu, X. Han, B.F. Spencer, M.D. Frogley, F. Tuna, E.J. L. McInnes, R.A.W. Dryfe, B. Han, S. Yang, M. Schroder, Quantitative electroreduction of CO₂ to liquid fuel over electro-synthesized metal-organic frameworks, *J. Am. Chem. Soc.* 142 (2020) 17384–17392.
- [12] B. Pan, G. Yuan, X. Zhao, N. Han, Y. Huang, K. Feng, C. Cheng, J. Zhong, L. Zhang, Y. Wang, Y. Li, Highly dispersed indium oxide nanoparticles supported on carbon nanorods enabling efficient electrochemical CO₂ reduction, *Small Sci.* 1 (2021), 2100029.
- [13] T. Zheng, C. Liu, C. Guo, M. Zhang, X. Li, Q. Jiang, W. Xue, H. Li, A. Li, C.-W. Pao, J. Xiao, C. Xia, J. Zeng, Copper-catalysed exclusive CO₂ to pure formic acid conversion via single-atom alloying, *Nat. Nanotechnol.* 16 (2021) 1386–U1394.
- [14] N. Han, P. Ding, L. He, Y.Y. Li, Y.G. Li, Promises of main group metal-based nanostructured materials for electrochemical CO₂ reduction to formate, *Adv. Energy Mater.* 10 (2020), 1902338.
- [15] T.-P. Thanh, R. Daiyan, Z. Fusco, Z. Ma, R. Amal, A. Tricoli, Nanostructured beta-Bi₂O₃ fractals on carbon fibers for highly selective CO₂ electroreduction to formate, *Adv. Funct. Mater.* 30 (2020), 1906478.
- [16] S.S. He, F.L. Ni, Y.J. Ji, L.E. Wang, Y.Z. Wen, H.P. Bai, G.J. Liu, Y. Zhang, Y.Y. Li, B. Zhang, H.S. Peng, The p-orbital delocalization of main-group metals to boost CO₂ electroreduction, *Angew. Chem. Int. Ed.* 57 (2018) 16114–16119.
- [17] H. Wang, Nanostructure@metal-organic frameworks (MOFs) for catalytic carbon dioxide (CO₂) conversion in photocatalysis, electrocatalysis, and thermal catalysis, *Nano Res.* (2021), <https://doi.org/10.1007/s12274-12021-13984-12279>.
- [18] P. Deng, F. Yang, Z. Wang, S. Chen, Y. Zhou, S. Zaman, B.Y. Xia, Metal-organic framework-derived carbon nanorods encapsulating bismuth oxides for rapid and selective CO₂ electroreduction to formate, *Angew. Chem. Int. Ed.* 59 (2020) 10807–10813.
- [19] W.W. Yuan, J.X. Wu, X.D. Zhang, S.Z. Hou, M. Xu, Z.Y. Gu, In situ transformation of bismuth metal-organic frameworks for efficient selective electroreduction of CO₂ to formate, *J. Mater. Chem. A* 8 (2020) 24486–24492.
- [20] N.H. Li, P. Yan, Y.H. Tang, J.H. Wang, X.Y. Yu, H. Bin Wu, In-situ formation of ligand-stabilized bismuth nanosheets for efficient CO₂ conversion, *Appl. Catal. B-Environ.* 297 (2021), 120481.
- [21] C.S. Cao, D.D. Ma, J.F. Gu, X.Y. Xie, G. Zeng, X.F. Li, S.G. Han, Q.L. Zhu, X.T. Wu, Q. Xu, Metal-organic layers leading to atomically thin bismuthene for efficient carbon dioxide electroreduction to liquid fuel, *Angew. Chem. Int. Ed.* 59 (2020) 15014–15020.
- [22] Y. Ying, B. Khezri, J. Kosina, M. Pumera, Reconstructed bismuth-based metal-organic framework nanofibers for selective CO₂-to-formate conversion: morphology engineering, *ChemSusChem* 14 (2021) 3402–3412.
- [23] D. Yao, C. Tang, The controllable reconstruction of Bi-MOFs for electrochemical CO₂ reduction through electrolyte and potential mediation, *Angew. Chem. Int. Ed.* 60 (2021) 2–9.
- [24] C.-J. Peng, G. Zeng, D.-D. Ma, C. Cao, S. Zhou, X.-T. Wu, Q.-L. Zhu, Hydrangea-like superstructured micro/nanoreactor of topotactically converted ultrathin bismuth nanosheets for highly active CO₂ electroreduction to formate, *ACS Appl. Mater. Interfaces* 13 (2021) 20589–20597.
- [25] T. Ma, Z. Wu, H. Wu, W. Cai, Z. Wen, L. Wang, W. Jin, B. Jia, Engineering Bi-Sn interface in bimetallic aerogel with 3D porous structure for highly selective electrocatalytic CO₂ reduction to HCOOH, *Angew. Chem. Int. Ed.* 60 (2021) 12554–12559.

- [26] Y. Xing, X. Kong, X. Guo, Y. Liu, Q. Li, Y. Zhang, Y. Sheng, X. Yang, Z. Geng, J. Zeng, Bi@Sn core-shell structure with compressive strain boosts the electroreduction of CO₂ into formic acid, *Adv. Sci.* 7 (2020), 1902989.
- [27] G. Wen, D.U. Lee, B. Ren, F.M. Hassan, G. Jiang, Z.P. Cano, J. Gostick, E. Croiset, Z. Bai, L. Yang, Z. Chen, Orbital interactions in Bi-Sn bimetallic electrocatalysts for highly selective electrochemical CO₂ reduction toward formate production, *Adv. Energy Mater.* 8 (2018), 1802427.
- [28] L. Li, A. Ozden, S. Guo, F.P. Garci, A. de Arquer, C. Wang, M. Zhang, J. Zhang, H. Jiang, W. Wang, H. Dong, D. Sinton, E.H. Sargent, M. Zhong, Stable, active CO₂ reduction to formate via redox-modulated stabilization of active sites, *Nat. Commun.* 12 (2021) 5223.
- [29] Y.-X. Duan, Y.-T. Zhou, Z. Yu, D.-X. Liu, Z. Wen, J.-M. Yan, Q. Jiang, Boosting production of HCOOH from CO₂ electroreduction via Bi/CeO_x, *Angew. Chem. Int. Ed.* 60 (2021) 8798–8802.
- [30] J. Albo, M. Perfecto-Irigaray, G. Beobide, A. Irabien, Cu/Bi metal-organic framework-based systems for an enhanced electrochemical transformation of CO₂ to alcohols, *J. CO₂ Util.* 33 (2019) 157–165.
- [31] B. Wei, Y.S. Xiong, Z.Y. Zhang, J.H. Hao, L.H. Li, W.D. Shi, Efficient electrocatalytic reduction of CO₂ to HCOOH by bimetallic In-Cu nanoparticles with controlled growth facet, *Appl. Catal. B-Environ.* 283 (2021) 11.
- [32] P. Lu, X. Tan, H. Zhao, Q. Xiang, K. Liu, X. Zhao, X. Yin, X. Li, X. Hai, S. Xi, A.T. S. Wee, S.J. Pennycook, X. Yu, M. Yuan, J. Wu, G. Zhang, S.C. Smith, Z. Yin, Atomically dispersed indium sites for selective CO₂ electroreduction to formic acid, *Acs Nano* 15 (2021) 5671–5678.
- [33] H. Shang, T. Wang, J. Pei, Z. Jiang, D. Zhou, Y. Wang, H. Li, J. Dong, Z. Zhuang, W. Chen, D. Wang, J. Zhang, Y. Li, Design of a single-atom indium(δ+)-N₄ interface for efficient electroreduction of CO₂ to formate, *Angew. Chem. Int. Ed.* 59 (2020) 22465–22469.
- [34] X. Li, Y. Sun, J. Xu, Y. Shao, J. Wu, X. Xu, Y. Pan, H. Ju, J. Zhu, Y. Xie, Selective visible-light-driven photocatalytic CO₂ reduction to CH₄ mediated by atomically thin CuIn₂S₄ layers, *Nat. Energy* 4 (2019) 690–699.
- [35] Y.D. Zhang, T.T. Hou, Q. Xu, Q.Y. Wang, Y. Bai, S.K. Yang, D.W. Rao, L.H. Wu, H. B. Pan, J.F. Chen, G.M. Wang, J.F. Zhu, T. Yao, X.S. Zheng, Dual-metal sites boosting polarization of nitrogen molecules for efficient nitrogen photofixation, *Adv. Sci.* 8 (2021), 2100302.
- [36] Y. Fu, T. Li, G. Zhou, J. Guo, Y. Ao, Y. Hu, J. Shen, L. Liu, X. Wu, Dual-metal-driven selective pathway of nitrogen reduction in orderly atomic-hybridized Re₂MnS₆ ultrathin nanosheets, *Nano Lett.* 20 (2020) 4960–4967.
- [37] J.J. Pei, T. Wang, R. Sui, X.J. Zhang, D.N. Zhou, F.J. Qin, X. Zhao, Q.H. Liu, W. S. Yan, J.C. Dong, L.R. Zheng, A. Li, J.J. Mao, W. Zhu, W.X. Chen, Z.B. Zhuang, N-bridged Co-N-Ni: new bimetallic sites for promoting electrochemical CO₂ reduction dagger, *Energy Environ. Sci.* 14 (2021) 3019–3028.
- [38] W. Luc, J. Rosen, F. Jiao, An Ir-based anode for a practical CO₂ electrolyzer, *Catal. Today* 288 (2017) 79–84.
- [39] Kresse, Furthmuller, Efficient iterative schemes for ab initio total-energy calculations using a plane-wave basis set, *Phys. Rev. B* 54 (1996) 11169–11186.
- [40] Kresse, Hafner, Ab initio molecular-dynamics simulation of the liquid-metal-amorphous-semiconductor transition in germanium, *Phys. Rev. B* 49 (1994) 14251–14269.
- [41] Perdew, Chevary, Vosko, Jackson, Pederson, Singh, Fiolhais, Atoms, molecules, solids, and surfaces: applications of the generalized gradient approximation for exchange and correlation, *Phys. Rev. B* 46 (1992) 6671–6687.
- [42] Burke, Perdew, Ernzerhof, Generalized gradient approximation made simple, *Phys. Rev. Lett.* 77 (1996) 3865–3868.
- [43] Methfessel, Paxton, High-precision sampling for Brillouin-zone integration in metals, *Phys. Rev. B* 40 (1989) 3616–3621.
- [44] G. Wang, Y. Liu, B. Huang, X. Qin, X. Zhang, Y. Dai, A novel metal-organic framework based on bismuth and trimesic acid: synthesis, structure and properties, *Dalton Trans.* 44 (2015) 16238–16241.
- [45] B. Lu, S. Wang, L. Zhao, D. Zhou, S. Dong, G. Wang, Selective and superior capture of phosphate by using bimetallic bismuth-based metal-organic frameworks, *Chem. Eng. J.* 425 (2021), 131514.
- [46] S. Dhanasingh, D. Nallasamy, S. Padmanapan, V.C. Padaki, Cetyltrimethylammonium bromide- and ethylene glycol-assisted preparation of mono-dispersed indium oxide nanoparticles using hydrothermal method, *Chem. Pap.* 68 (2014) 1079–1086.
- [47] Y.B. Zhao, Z.J. Zhang, W.M. Liu, H.X. Dang, Q.J. Xue, Controlling synthesis of Biln dendritic nanocrystals by solution dispersion, *J. Am. Chem. Soc.* 126 (2004) 6854–6855.
- [48] Q. Yang, Q. Wu, Y. Liu, S. Luo, X. Wu, X. Zhao, H. Zou, B. Long, W. Chen, Y. Liao, L. Li, P.K. Shen, L. Duan, Z. Quan, Novel Bi-doped amorphous SnO_x nanoshells for efficient electrochemical CO₂ reduction into formate at low overpotentials, *Adv. Mater.* 32 (2020), 2002822.
- [49] K. Yao, Y. Xia, J. Li, N. Wang, J. Han, C. Gao, M. Han, G. Shen, Y. Liu, A. Seifitokaldani, X. Sun, H. Liang, Metal-organic framework derived copper catalysts for CO₂ to ethylene conversion, *J. Mater. Chem. A* 8 (2020) 11117–11123.
- [50] Y. Xu, J.P. Edwards, S.J. Liu, R.K. Miao, J.E. Huang, C.M. Gabardo, C.P. O'Brien, J. Li, E.H. Sargent, D. Sinton, Self-cleaning CO₂ reduction systems: unsteady electrochemical forcing enables stability, *ACS Energy Lett.* 6 (2021) 809–815.
- [51] Y. Yang, X. Li, F. Tang, P. Ming, B. Li, C. Zhang, Power evolution of fuel cell stack driven by anode gas diffusion layer degradation, *Appl. Energy* 313 (2022), 118858.
- [52] C. Xia, P. Zhu, Q. Jiang, Y. Pan, W.T. Liang, E. Stavitsk, H.N. Alshareef, H.T. Wang, Continuous production of pure liquid fuel solutions via electrocatalytic CO₂ reduction using solid-electrolyte devices, *Nat. Energy* 4 (2019) 776–785.
- [53] Y. Kim, S. Park, S.-J. Shin, W. Choi, B.K. Min, H. Kim, W. Kim, Y.J. Hwang, Time-resolved observation of C-C coupling intermediates on Cu electrodes for selective electrochemical CO₂ reduction, *Energy Environ. Sci.* 13 (2020) 4301–4311.
- [54] Z.-H. Zhu, B.-H. Zhao, S.-L. Hou, X.-L. Jiang, Z.-L. Liang, B. Zhang, B. Zhao, A facile strategy for constructing a carbon-particle-modified metal-organic framework for enhancing the efficiency of CO₂ electroreduction into formate, *Angew. Chem. Int. Ed.* 60 (2021) 23394–23402.
- [55] S. Zhu, B. Jiang, W.-B. Cai, M. Shao, Direct observation on reaction intermediates and the role of bicarbonate anions in CO₂ electrochemical reduction reaction on Cu surfaces, *J. Am. Chem. Soc.* 139 (2017) 15664–15667.
- [56] A. Zhang, Y. Liang, H. Li, X. Zhao, Y. Chen, B. Zhang, W. Zhu, J. Zeng, Harmonizing the electronic structures of the adsorbate and catalysts for efficient CO₂ reduction, *Nano Lett.* 19 (2019) 6547–6553.